

Chapter 2

The Cosmic Rays and Our Galaxy

Primary *Cosmic Rays* (CRs) are fully ionized atomic nuclei and other particles accelerated at astrophysical sources and reaching the Earth. In this book, usually we indicate with the acronym “CRs” protons and nuclei in the cosmic radiation. The electron, γ -ray, and neutrino components of CRs will be always specified. The discovery of CRs (Sects. 2.1 and 2.2) made it possible to verify both the Einstein relation between particle’s mass and energy and the Dirac theory about the existence of antimatter (Sect. 2.3). Particle detectors play (Sect. 2.4) a fundamental role in this history.

Some quantitative aspect of the CRs, as the differential and integral flux, are defined in Sect. 2.5 and the measured energy spectrum of the primary cosmic rays are presented in Sect. 2.6. Most CRs originate outside the solar system and the physical properties of the Galaxy (dimension, matter density, magnetic fields, described in Sect. 2.7) have an effect on their journey from sources to the Earth. Only low-energy particles (below few GeV) are of solar origin (Sect. 2.8). The intensity of this ionizing radiation is modulated by the solar activity. Below few tens of GeV, the primary CR flux depends also from the magnetic latitude as it is affected by the geomagnetic field (Sect. 2.9).

The theoretical models on the origin of CRs rely on many astrophysical parameters and experimental observations about nature, energy density, confinement time, and chemical composition of CRs as a function of their energy. Supernova remnants are recognized as candidates for the acceleration of galactic CRs. The main motivation is the relation (described in Sect. 2.11) between the loss in kinetic energy due to CRs escape from the galactic disk and the energy released by supernova shock waves. The details of the physical mechanisms through which kinetic energy is transferred to high-energy particles will be described in Chap. 6.

2.1 The Discovery of Cosmic Rays

The discovery of CRs is commonly attributed to Victor Hess (1912). After the discovery of radioactivity in 1896 by Henri Becquerel, while studying phosphorescent materials, it was known that some materials can produce *ionizations*. These

substances are called *radioactive materials*, for their similarity with the radium (^{88}Ra). In the presence of a radioactive material, a charged *electroscope* promptly discharges, while their golden leaves can stay apart from each other if the ionization level of the surrounding material is low. Radioactive elements emit charged particles, which ionize the gas therein, thus causing the discharge of electroscopes. The discharge rate was used at the beginning of the last century to measure the level of radioactivity.

Around 1900, Wilson and others developed a new technique for the insulation of electroscopes in a closed vessel, thus improving the sensitivity of the electroscope itself. As the discharge was present also when no radioactive elements were present inside the electroscope shielding, the presence of ionizing agents coming from outside the vessel was assumed. The questions concerned the Earth or the extraterrestrial origin of such radiation. An experimental confirmation of one of the two hypotheses, however, seemed hard to achieve.

The original idea to perform a measurement far from any terrestrial material seems to be due to Theodor Wulf. In 1909, using an improved electroscope in which two metalized silicon glass wires replaced the two golden leaves, Wulf measured the rate of ionization at the top of the Eiffel Tower in Paris (300 m above ground). According to the hypothesis of the terrestrial origin of most of the radiation, a smaller ionization rate was expected at the top of the tower than on ground. The measured ionization rate was, however, too similar to that on ground to allow a confirmation of the extraterrestrial origin of a part of the radiation.

The first measurement using a balloon (by K. Bergwitz) was made in the same year: the ionization at 1,300 m altitude was found to be only about 24 % than ground level. The final answer to the problem was given by the Austrian physicist Victor Hess (Fig. 2.1). After many balloon flights (starting from 1911) and different instruments on board, finally in 1912 he reached an altitude of 5,200 m. The results clearly showed that the ionization, after going through a minimum, increased considerably with height. Hess concluded that the increase of the ionization with height was originated by radiation coming from space. He also noticed the absence of day–night variations and thus he excluded the Sun as the direct source of this hypothetical penetrating radiation.

The results by Hess were later confirmed by W. Kolhörster in a number of flights up to 9,200 m. Hess was awarded the Nobel Prize in physics in 1936 for the discovery of the *cosmic rays*.

It should also be mentioned that several important contributions to the discovery of the origin of CRs have been forgotten. In particular that of D. Pacini, who in an earlier paper (Pacini 1912) wrote (in Italian) that *a sizable cause of ionization exists in the atmosphere, originating from penetrating radiation, independent of the direct action of radioactive substances in the soil*. A recommended historical overview of the early age of the history of cosmic rays is in Carlson and De Angelis (2010) and references therein.

After the discovery of CRs, a long scientific debate started about the nature of such an extraterrestrial radiation. Most believed at the beginning that cosmic rays were γ -rays because of their huge penetrating power. In particular, R.A. Millikan

Fig. 2.1 Historical photograph of Hess preparing for a balloon flight (American Physical Society)



hypothesized that those extraterrestrial γ -rays were produced during the formation of helium nuclei in the interstellar space, starting from the combination of protons and electrons.

In 1927, J. Clay found evidence of a variation of the cosmic ray intensity with latitude. As this deflection was attributed to the presence of the geomagnetic field, the only plausible interpretation was that the primary cosmic rays were charged particles, not photons. This interpretation was principally due to Bruno Rossi, who in 1930 predicted a difference between the intensities of CRs arriving from the East and the West assuming positively charged particles. A world-wide survey was performed in 1932 by Compton, which verified the Rossi prediction of the so-called “East-West effect” and rejected the Millikan theory.

In 1938–1939 (in Paris first and then in the Alps mountains), P. Auger and collaborators showed that groups of particles could arrive in time coincidence on detectors separated by distances as large as 200 m. This was the first indication that the observed particles in atmosphere were secondary particles induced from a common primary CR (Auger et al. 1939). They concluded that there exist in the Universe mechanisms able to accelerate particles up to an energy of 10^{15} eV. Note that at that time the largest energies from natural radioactivity or artificial acceleration were just a few MeV. Only in 1941 it was established (Schein et al. 1941) that CRs were mostly protons.

In 1962, John Linsley observed an event interpreted due to a cosmic ray of energy 10^{20} eV (Linsley 1962). This event was measured by an array of scintillation counters spread over 8 km^2 in a desert of New Mexico (USA).

2.2 Cosmic Rays and the Early Days of Particle Physics

CRs are very-high-energy particles entering the atmosphere, making it possible before the advent of particle accelerators the creation of new, unstable particles through the Einstein relation between *energy* and *mass*. Around 1920, only the proton, the electron, and the photon were known as *elementary particles*. Before the advent of particles accelerators, up to the 1950s, the study and discovery of new particles and the study of the fundamental interactions between elementary particles was performed mainly using cosmic rays.

Since the 1930s, the experimental techniques for the detection and measurement of some physical quantities (e.g., electric charge, mass, lifetime) of the particles present in the secondary cosmic rays started to become more refined. Particularly, P. Blackett (Nobel laureate in 1948) used a cloud chamber inside a magnetic field that bent the trajectory of charged particles. Experimental techniques using CRs remained useful until well after the end of the Second World War, when particle accelerators started to be developed.

Using Blackett's experimental techniques, in 1932, C. Anderson (Nobel laureate in 1936) discovered a particle having the same mass as the electron, though with opposite electric charge (Fig. 2.2). It was the *antielectron* (or *positron*), that is, the antiparticle predicted by the relativistic quantum theory of the electron developed a few years before by P.A.M. Dirac (Nobel laureate in 1933). Immediately afterwards, in 1934, J. Chadwick (Nobel laureate in 1935) experimentally identified a particle with a mass similar to that of the proton, though without electric charge: the neutron.

In 1937, C. Anderson and S. Neddermeyer discovered a particle of intermediate mass between that of the proton and of the electron: they called this new particle the *meson*. For some time, it was thought that this particle was that necessary to glue protons and neutrons in nuclei. A theoretical model due to H. Yukawa (Nobel laureate in 1949) predicted the existence of a particle with a mass very close to that of the just discovered meson. Nevertheless, during World War II in Rome, M. Conversi, E. Pancini and O. Piccioni demonstrated in a famous experiment using secondary cosmic rays that the meson of Anderson and Neddermeyer (nowadays called the *muon*) was not the particle predicted by Yukawa. Even if the theory of Yukawa does not properly describe the physics of nuclei, the predicted particle (the *pion*) was discovered in 1947 by C. Lattes, G. Occhialini and G. Powell in secondary cosmic rays using nuclear emulsions (i.e., sophisticated photographic films) at high altitudes.

In 1947, in the interactions of cosmic rays in a cloud chamber with magnetic field, particles with a particularly strange behavior were discovered. They were thus named *strange* particles. Many years later [see Chap. 7 of Braibant et al. (2011)], it

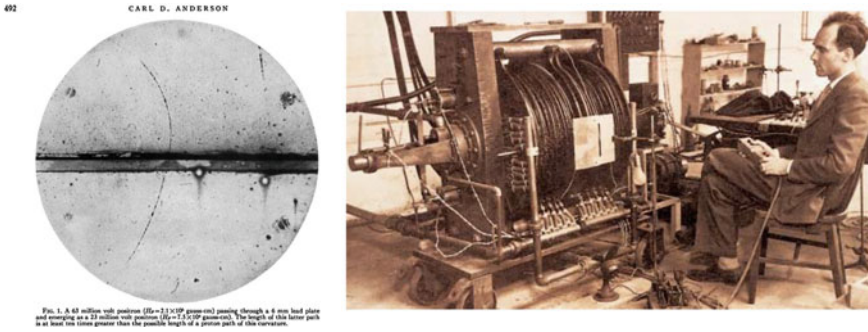


Fig. 2.2 *Left* The first image of a positron obtained by Anderson in a cloud chamber (Anderson 1933). A charged particle interacting with the supersaturated vapor of the mixture inside the chamber produces ionization. The resulting ions act as condensation centers, around which a mist will form. Due to many ions being produced along the path of the charged particle, the tracks of particles having electric charge $Ze = 1$ or 2 have distinctive shapes (an alpha particle's track is broad, while an electron's is thinner and straight). The particle in this event has the same electric charge of the electron but opposite sign, Sect. 2.3. *Right* Carl D. Anderson, Nobel Prize for Physics in 1936, with its detector: a cloud chamber inside an electromagnet

was realized that strange particles, as protons and neutrons, are composite objects. Protons and neutrons, and other short-lived particles with semi-integer spin, are made of three u and d quarks. The pions, as other mesons with null or integer spin, are made of a quark and an antiquark. Strange particles contain a new, heavier quark called s (for *strange*). With the advent of accelerators, the fields of particle physics and that of cosmic rays parted ways, though they have actually reconnected in recent years.

2.3 The Discovery of the Positron and Particle Detectors

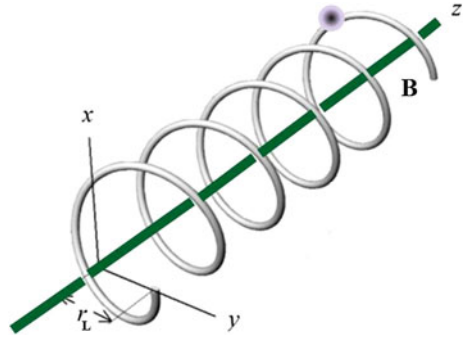
In this section, we will use the Anderson's picture of the detected positron to introduce how particles are identified with the help of an external magnetic field.

2.3.1 The Motion in a Magnetic Field and the Particle Rigidity

The Lorentz force exerted by the magnetic field \mathbf{B} on a particle with charge q , mass m , and velocity \mathbf{v} is (in c.g.s. units)

$$\Gamma m \frac{d\mathbf{v}}{dt} = \frac{q}{c} \mathbf{v} \times \mathbf{B} \quad (2.1)$$

Fig. 2.3 The motion of a charged particle along the \mathbf{B} field line



where Γ^1 is the Lorentz factor:

$$\Gamma \equiv \frac{1}{\sqrt{1 - v^2/c^2}} = \frac{E}{mc^2} . \quad (2.2)$$

Since the acceleration is perpendicular to both the magnetic field and velocity vectors, in the case of a static uniform field, the orbit is a circle, plus a uniform motion along the direction of \mathbf{B} . The resulting helicoidal motion is shown in Fig. 2.3. The integration of Eq. (2.1) yields for a static and uniform magnetic field:

$$\mathbf{v} = \mathbf{r} \times \frac{q\mathbf{B}}{\Gamma mc} \equiv \mathbf{r} \times \boldsymbol{\omega}_L . \quad (2.3)$$

The angular frequency of the circular motion is

$$\omega_L = \frac{2\pi}{T_L} = \frac{qB}{\Gamma mc} . \quad (2.4)$$

The radius of the orbit is called the *cyclotron radius* or *Larmor radius*. For $q = Ze$, where e is the electric charge of the proton,² the Larmor radius is:

$$r_L = \frac{v}{\omega_L} = \frac{\Gamma m v c}{ZeB} = \frac{pc}{ZeB} \simeq \frac{E}{ZeB} \quad (2.5)$$

The last equality holds only for relativistic particles (as in most cases in this textbook). The cyclotron radius decreases with the increase of the charge Z of a nucleus, in units of the proton electric charge. As the effect of a magnetic field on a particle depends

¹ In the book, we use the Γ (uppercase) for the Lorentz factor to avoid confusion with the γ -ray.

² A major difference between the c.g.s. and SI units is in the definition of the unit of charge. The c.g.s. unit of electrical charge (the statcoulomb, statC) can be written entirely as a dimensional combination of the mechanical units (gram, centimeter, second). In this book, we use the notation that $e = 4.8 \times 10^{-10}$ statC is the proton charge; $-e$ will be the electron charge.

on the ratio between momentum and electric charge, the particle *rigidity* R is defined as:

$$R \equiv \frac{pc}{Ze} \simeq \frac{E}{Ze} = \frac{1.6 \times 10^{-12}(\text{eV/erg})E(\text{erg})}{4.8 \times 10^{-12}(\text{statC})} = \frac{1}{300}E \quad [\text{V}] \quad (2.6)$$

when the energy is measured in eV. By definition, the eV is the product of an electric charge and a potential difference, and the rigidity is measured in Volts. If a multiple of the eV is used (for instance, the GeV), the rigidity is automatically expressed in the same multiple (GV).

2.3.2 The Identification of the Positron

Let us consider the picture in Fig. 2.2. The additional information which we have are:

- a 6 mm-thick lead plate is located in the middle of the chamber. A particle, while crossing the plate, losses energy;
- the intensity of the magnetic field inside the electromagnet in the region of the cloud chamber is 15 kG;
- the magnetic field is perpendicular to the plane of the paper;
- by comparing the number of ionization centers in the chamber with that released by radioactive nuclei emitting α (helium nuclei with charge $= 2e$) or β radiation, the particle has an electric charge $+e$ or $-e$.

The simplest interpretation (an electron with charge $-e$ entering from above) is wrong. To demonstrate it, we draw in Fig. 2.4 two circles which interpolate the ionization points before and after the lead layer. The picture represents the projection on a plane of the 3-D particle trajectory³ and our drawing is only approximate. In any case, we are lucky enough that the trajectory of the particle is mainly in the plane of the picture. Observing the circles, it is evident that the radius of curvature is larger in the bottom region. From (2.5), we conclude that the energy of the particle is larger in the region below the lead. Thus:

- the particle must have entered the chamber from below;

As we know the directions of the particle velocity and of the magnetic field (entering the plane), using the relation $\mathbf{F} \propto \mathbf{v} \times \mathbf{B}$ we obtain that

- the particle has suffered a force toward the left. Thus, it is a positively charged particle.

It remains to show that

³ For these reasons, in later *bubble chamber* techniques two or more views of the event were used.

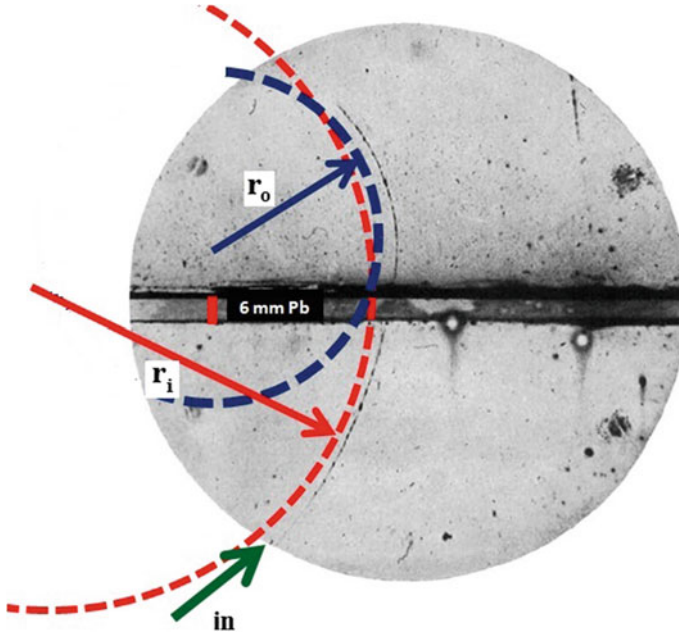


Fig. 2.4 The Anderson's positron picture interpolated with two *arcs of circle* (slightly shifted to the *left*, to show the original track). The energy loss in the Pb plate is that characteristic of an electron-like particle (see text). The fact that $r_o < r_i$ indicates that the particle energy is $E_o < E_i$ and thus that it enters from below (*arrow*). However, from the knowledge of the magnetic field direction, the sign of the charge of this particle must be positive. It cannot be an electron

- the particle in the figure cannot be a proton and has almost the same mass as the electron. Thus, is a *positron*, the particle foreseen by the quantum Dirac theory of the electron.

For this last step, we use the measurement of the radius of curvature of the two circles drawn in Fig. 2.4. The ruler in the figure is provided by the 6 mm Pb plate. The radius of the two circles can be scaled using this ruler in a way independent of the magnification of the picture. Our estimate is $r_i = 14$ cm, $r_o = 7$ cm for the particle when it enters and exits the cloud chamber, respectively. From (2.5), we obtain the respective particle momentum:

$$\begin{aligned} p_i c &= r_i e B = 14 \times (4.8 \times 10^{-10}) \times (1.5 \times 10^4) = 1.0 \times 10^{-4} \text{ erg} \\ p_i &= 63 \text{ MeV}/c \end{aligned} \quad (2.7a)$$

using the relation $1 \text{ erg} = 1.6 \times 10^{-12} \text{ eV}$. Similarly, after the plate⁴:

⁴ In his work (Anderson 1933), Anderson reported a 63 million volt positron passing through a 6 mm lead plate and emerging as a 23 million volt positron. Our result is not so bad.

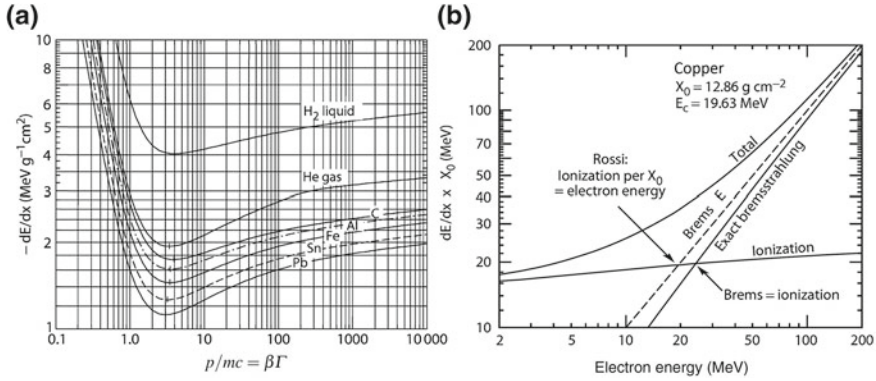


Fig. 2.5 **a** Mean energy loss in different materials of charged particles due to the electromagnetic interactions (excitation and ionization) with the electrons of the medium. The *horizontal scale* is in $\beta\Gamma$ units, which is independent of the incident particle type. **b** Electron energy loss in copper as a function of the electron energy. The excitation and ionization contribution remains roughly constant with increasing energy. Instead, the term due to the electron energy loss through interactions with nuclei (bremsstrahlung) increases. The intersecting point of the two curves defines the critical energy. In this figure, it corresponds to about 20 MeV. *Credit* the Particle Data Group (Beringer et al. 2012)

$$p_o = r_o e B / c = 32 \text{ MeV}/c \quad (2.7b)$$

The energy loss of charged particles through excitation and ionization of a material is given by the Bethe-Bloch formula as a function of the particle momentum p . It depends on the charge Ze and velocity $\beta = v/c$ of the incoming particle and only weakly from the properties of the crossed material. When p is expressed in terms of the adimensional Lorentz factors $p/mc = \beta\Gamma$, the energy loss assumes the behavior shown in Fig. 2.5a. The energy loss curves have a minimum for $\beta\Gamma \simeq 3$, that is, $pc = 3mc^2$. Neglecting the logarithmic rise when $E \sim pc \gg mc^2$, the Bethe-Bloch formula can be approximated as:

$$-\frac{dE}{dx} = \frac{Z^2}{\beta^2} \left(\frac{dE}{dx} \right)_{\min} ; \quad \text{with} \quad \left(\frac{dE}{dx} \right)_{\min} \simeq 2 \text{ MeV g}^{-1} \text{cm}^2 \quad (2.8)$$

Let us consider the energy loss under the hypothesis of an incoming proton ($m_p c^2 = 938 \text{ MeV}$) with momentum p_i and

$$\beta\Gamma = \frac{p_i c}{m_p c^2} = \frac{63 \text{ MeV}}{938 \text{ MeV}} \simeq 0.07. \quad (2.9)$$

The energy loss for such a low momentum is outside the scale of Fig. 2.5a. The energy loss can be estimated from (2.8), assuming $\beta\Gamma \sim \beta = 0.07$. The specific energy loss in lead (density $\rho_{\text{Pb}} = 11 \text{ g cm}^{-3}$) corresponds to

$$-\frac{dE}{dx} = (0.07)^{-2} \times 2 \text{ (MeV cm}^2\text{/g)} \times 11 \text{ (g cm}^{-3}\text{)} \simeq 5,000 \text{ MeV/cm.}$$

To cross 6 mm of lead, a proton would lose $\sim 3,000 \text{ MeV}$. This is by far inconsistent with the observed variation of energy $\Delta E = E_i - E_o = 1.5 \text{ MeV}$, assuming an incoming proton having $p_i = 63 \text{ MeV/c}$ and $p_o = 32 \text{ MeV/c}$. The positively charged particle in the picture cannot thus be a proton!

Let us consider the case of a *positive electron*. From the Dirac theory, its mass is identical to that of the electron ($m_e c^2 = 0.511 \text{ MeV}$), so that:

$$\beta\Gamma = \frac{p_i c}{m_e c^2} = \frac{63 \text{ MeV}}{0.511 \text{ MeV}} \simeq 123 \quad (2.10)$$

In the case of the electron, in addition to the excitation-ionization energy loss, also the *bremsstrahlung* (hard Coulomb scattering with atomic nuclei) process must be considered. The electron energy loss in copper is given in Fig. 2.5b. Copper has a radiation length $X_0 \sim 12.9 \text{ g cm}^{-2}$, Sect. 3.3. From the figure, to an electron with $p = 63 \text{ MeV/c}$ corresponds an energy $E = 63 \text{ MeV}$ and thus:

$$\frac{dE}{dx} \times X_0 \simeq 70 \text{ MeV} \rightarrow \frac{dE}{dx} \simeq 70/12.9 = 5.4 \text{ MeV/g cm}^{-2}$$

Thus, assuming the usual 6 mm of lead i.e. $\Delta x = 6.6 \text{ g cm}^{-2}$:

$$\Delta E \sim 5.4 \times 6.6 = 36 \text{ MeV} . \quad (2.11)$$

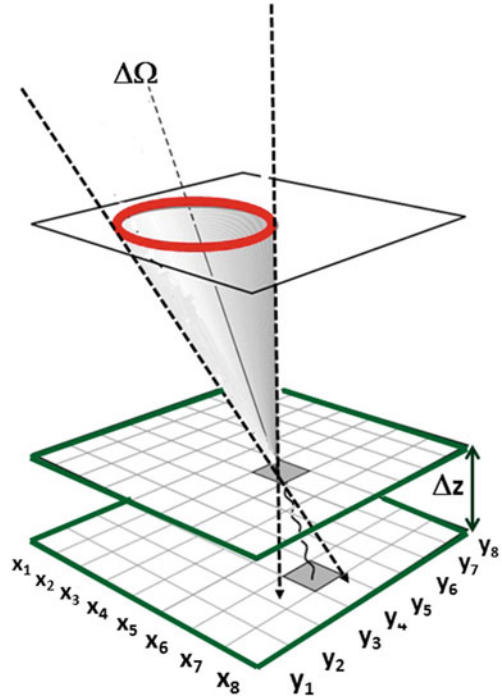
As the electron is relativistic, the energy loss from the picture is simply $E_i - E_o \simeq p_i c - p_o c = 31 \text{ MeV}$ in the 6 mm of lead, very close to the value obtained using (2.11). The mass and energy loss properties of the particle are compatible with that of the electron!⁵

2.4 A Toy Telescope for Primary Cosmic Rays

The aforementioned example of the positron discovery, although using very simple devices, is an example of how detectors for particle identification operate. Any experimental apparatus for CRs detection should: (i) identify the particle, (ii) measure its electric charge, and (iii) measure its energy and momentum. We illustrate in the following how the *flux* of particles can be measured with a simple experimental device. The techniques used by modern experiments for the direct measurement of CRs are presented in the next chapter.

⁵ At the time of the Anderson picture, only protons and electrons were known as charged particles. Try to work out that the observed particle cannot be a charged π^+ meson, with $m_\pi = 139.6 \text{ MeV/c}^2$.

Fig. 2.6 Layout of a simple telescope for the measurement of CRs. The two counter's layers are assumed to be segmented both in the x and y axis. A CR arriving within the *solid angle* $\Delta\Omega$ will produce one hit on each *layer* (see text)



Our ideal experiment (a *toy telescope for charged CRs*) is made of two layers of counters of a given area A separated by the distance Δz (see Fig. 2.6). Each counter's layer is segmented with a characteristic spatial resolution. The signal in the counter is provided by the excitation/ionization energy loss of through-going charged particles, see Chap. 2 of Braibant et al. (2011). The excitation/ionization energy loss (2.8) is proportional to the square of the electric charge Z of the particle. With *proportional counters* the *amplitude* I of the signal depends thus on Z^2 . This method to measure the electric charge of the incoming particle through Eq. (2.8) will be referred in the following as *dE/dx measurement*. Primary CRs can be measured if the telescope is carried to the top of the atmosphere by a balloon or outside the atmosphere by a satellite.

In Fig. 2.6 we assume that a charged particle crossing the lower counter induces a signal at the position labeled (x_7, y_4) . Additional information are the z -position z_1 of the layer, the crossing time (t_1) and the amplitude I_1 of the signal. The complete set of information (a *hit*) can be represented as $(x_7, y_4; z_1, t_1, I_1)$. The hits are stored as digital information on a *online* computer.

Each particle detector has some advantage/disadvantage with respect to others: some of them have good spatial resolution and poor timing resolution, and vice versa [see Sect. 2.7 of Braibant et al. (2011)]. The design of a modern experiment is a compromise between the requirements necessary to have the best performances in

terms of physics results, and the cost, dimension, power dissipation, weight, etc. of each sub-detector.

A major requirement of any experiment is the *trigger logic*. This is a mandatory task, because the probability of a *fake signal* on a single counter is high. Due to the presence (for instance) of radioactive elements in the surrounding materials, or due to electronic noise, there are spurious signals in each detector plane with usually larger rates. By definition, these spurious hits are not correlated with a crossing particle and constitute the background.

In our simple example, a trigger is given by a *coincidence* between planes. This corresponds to have a signal both on the z_1 and z_2 layers within a given time interval T . A condition on amplitudes I_1, I_2 can also be added. The hits are permanently stored in the computer for further analysis if $|t_1 - t_2| \leq T$. The combination of signals in both planes, without constraints on time difference, will usually provide a too large event rate with respect to the real CR rate.

Relativistic particles in vacuum cover 1 m in ~ 3.3 ns. Typical distances Δz between layers in CR telescopes (as in our example) are of the order of 1–2 m. The timing resolution of the detectors must be of the order of a ns (or better) to have the possibility to distinguish between upward-(with $t_2 - t_1 > 0$) and downward-(with $t_2 - t_1 < 0$) going cosmic rays. In this case, a *time-of-flight* (ToF) measurement is performed. A very good timing resolution is characteristic for instance of most *scintillation counters*. Scintillation counters can be arranged in order to have sufficient spatial resolution to distinguish different directions (as in our telescope). In addition, their response depends on the ionization energy loss, and thus on the particle Z^2 . Many ToF systems are also used to measure the Z of the detected particle.

In many real detectors a uniform *magnetic field* in the region between the counters performing a ToF is present. The magnetic field allows the measurement of the particle momentum (if $|Ze|$ is known) and sign of the charge, as charged particles are deflected according to their *rigidity*. To measure the curved particle trajectory, additional detectors are needed inside the magnetic field region. If the magnetic field is along the y axis, $\mathbf{B} = B\hat{\mathbf{y}}$, the deflection is expected along the x -axis for particles entering with velocity along $\hat{\mathbf{z}}$. In this case, detectors with good spatial resolution inside the magnetic field (*tracking systems*) are used to accurately measure the x coordinate. The combination of the magnetic field and tracking detectors forms a *magnetic spectrometer*.

Finally, depending on some constraints (for instance, the total weight of the payload on a satellite or balloon) a *calorimeter* or other devices for the measurement of the particle energy can be added (see Chap. 3 for real experiments in space or in the upper atmosphere).

2.5 Differential and Integral Flux

The simple CR telescope of Fig. 2.6 is useful for the definition of the quantities related to the measurement of the number N of incident particles per unit time on the detector surface A at a given solid angle $d\Omega$. Usually, the area seen by particles

depends upon their arrival direction (corresponding to a given zenith and azimuth angles θ and ϕ , respectively) in a small angular region $d\Omega = \sin\theta d\phi d\theta$ and thus $A = A(\theta, \phi) = A(\Omega)$. The quantity:

$$A\Omega \equiv \int A(\Omega) \cdot d\Omega \quad [\text{cm}^2\text{sr}] \quad (2.12)$$

is called *the geometrical factor*. The event rate in a detector (i.e. the number of events per second) is given by the particle flux (see below) times the geometrical factor.

The intensity vs. energy is determined using detectors able to measure the energy of the incoming particle. Thus the number of CRs arriving in a given energy interval dE and solid angle $d\Omega$ represents the *differential intensity of particles of a given energy in the given solid angle*:

$$\Phi(E) \equiv \frac{d^2\varphi}{dEd\Omega}(E) \equiv \frac{dN}{A \cdot T \cdot d\Omega \cdot dE} \quad \frac{\text{particles}}{\text{cm}^2\text{sr s GeV}}. \quad (2.13)$$

Sometimes, particles can be measured only if their energy is larger than a given energy threshold E_0 . Equivalently, we could be interested in all particles measured with energy larger than E_0 . In both cases:

$$\Phi(>E_0) \equiv \frac{d\varphi}{d\Omega}(E) = \int_{E_0}^{\infty} \frac{d^2\varphi}{dEd\Omega} dE \quad \frac{\text{particles}}{\text{cm}^2\text{sr s}} \quad (2.14)$$

represents the *integral intensity of particles with energy $> E_0$* , i.e. the measurement of the CR intensity for particles with energy larger than the given threshold.

According to the literature, the quantities $\Phi(E)$ (2.13) and $\Phi(>E_0)$ (2.14) are sometime called the *differential flux* and the *integral flux* of particles, respectively. Note the different units in the two cases. In the following chapters an index could appear: for instance, Φ_{CR} , Φ_e , Φ_γ , Φ_ν will indicate the flux of primary CRs, electrons, gamma-rays and neutrinos, respectively. Nuclei correspond to an important fraction of CRs. If the detector can measure the electric charge $i = Ze$ of the incoming nucleus, the flux Φ_i of the particular nuclear species can be defined, as for instance in Fig. 3.10.

The arrival direction of CRs is largely isotropic. The particles' flux through a spherical surface is simply given by the integration over the solid angle of (2.14):

$$\frac{d\varphi}{dE}(E) = 4\pi \frac{d^2\varphi}{dEd\Omega}(E) = 4\pi \Phi(E) \quad \frac{\text{particles}}{\text{cm}^2\text{s GeV}}. \quad (2.15)$$

In most cases (as for our ideal experiment of Fig. 2.6) we are interested in the flux through a planar surface. The differential particles flux through a planar detector from one hemisphere is:

$$\mathcal{F}(E) = \int \frac{d^2\varphi}{dEd\Omega} \cos\theta d\Omega \quad \frac{\text{particles}}{\text{cm}^2\text{s GeV}} \quad (2.16)$$

$d\Omega$ is as usual the elemental solid angle, θ the angle between the vector perpendicular to the area A and the direction of the incoming particle. For isotropic radiation (as in the case of the primary CRs) the flux on a plane is:

$$\begin{aligned}\mathcal{F}(E) &= \Phi(E) \int_0^{2\pi} d\phi \int_0^{\pi/2} d\theta \sin\theta \cos\theta \\ &= \pi \Phi(E) \int_0^{\pi/2} d\theta \sin 2\theta = \pi \Phi(E) \frac{\text{particles}}{\text{cm}^2 \text{ s GeV}} .\end{aligned}\quad (2.17a)$$

Note that the form of the surface changes the numerical coefficient in front of Φ with respect to (2.15). Integrating (2.17a) over energies, we obtain the quantity:

$$\mathcal{F}(> E) = \pi \Phi(>E) \frac{\text{particles}}{\text{cm}^2 \text{ s}} . \quad (2.17b)$$

An important quantity in astrophysics is the *number density* (units: cm^{-3}) of CRs moving with velocity v . The number density corresponds to the number of particles present in a given volume at a given time. The setup of Fig. 2.6 for instance is continuously crossed by CRs at given rate. If we imagine of taking a snapshot of the particles present in the detector volume at a given time and counting them, we could derive the number density of particles in the detector volume.

Using dimensional arguments, the number density can be easily obtained from the integral flux (2.14) integrated over the solid angle and divided by the velocity (cm/s). It is easy to work out that for an isotropic flux the *particle number density* is:

$$n = \frac{4\pi}{v} \Phi(>E) \frac{\text{particles}}{\text{cm}^3} . \quad (2.18a)$$

If the flux is not isotropic, the integration over the solid angle gives a factor different from 4π . If the particle velocity are not constant, an integration over the velocity distribution spectrum is also needed.

Sometimes we are interested in the *differential number density* of cosmic rays. Using (2.13) we obtain:

$$\frac{dn}{dE} = \frac{4\pi}{v} \Phi(E) \frac{\text{particles}}{\text{GeV cm}^3} . \quad (2.18b)$$

In this book, we are dealing practically always with relativistic particles, and $v \simeq c$.

2.6 The Energy Spectrum of Primary Cosmic Rays

After more than 100 years of research, we know that the solar system is permanently bombarded by a flux of highly energetic particles. Their energies extend from the MeV range to 10^{20} eV. The primary component arriving on the top of the atmosphere includes all stable charged particles and nuclei. Also some unstable nuclei (with lifetimes larger than 10^6 years) are found. This (small) fraction of radioactive nuclei is important to estimate the *escape time* of CRs (Sect. 5.1).

Figure 1.4 shows the integral intensity of CRs as measured by a large number of different experiments, from small detectors on board of balloon and satellites to huge air shower arrays on ground, covering surfaces of more than $3,000 \text{ km}^2$. Each experiment has measured the integral flux (2.14) in a given energy interval. The analytic interpolation of all available data shown in Fig. 1.4 is usually referred to as the *integral energy spectrum*.

The distribution of the differential flux (2.13) covering the whole energy interval of CRs is usually referred as the *differential energy spectrum* (or simply the *energy spectrum*) of CRs and it is shown in Fig. 2.7.

The energy spectrum falls steeply as a function of energy. The integral flux (2.17b) corresponding to different energy thresholds gives

$$\mathcal{F}(> 10^9 \text{ eV}) \simeq 1,000 \text{ particles/s m}^2 \quad (2.19a)$$

$$\mathcal{F}(> 10^{15} \text{ eV}) \simeq 1 \text{ particle/year m}^2 \quad (2.19b)$$

$$\mathcal{F}(> 10^{20} \text{ eV}) \simeq 1 \text{ particle/century km}^2. \quad (2.19c)$$

Figure 2.7 seems almost featureless, but two transition points (where the slope of the spectrum changes) are clearly visible. This feature defines three energy intervals in the CR spectrum. The transition point at $\sim 3 \times 10^6 \text{ GeV}$ is called the *knee*. Below the knee, the integral CR flux decreases by a factor ~ 50 when the energy increases by an order of magnitude.

At energies larger than few GeV (where the contribution of particles coming from the Sun, Sect. 2.8, is negligible) the energy spectrum can be described by a power-law:

$$\Phi(E) = K \left(\frac{E}{1 \text{ GeV}} \right)^{-\alpha} \frac{\text{particles}}{\text{cm}^2 \text{ s sr GeV}} \quad (2.20a)$$

$$\Phi(>E) = \frac{K}{(\alpha - 1)} \left(\frac{E}{1 \text{ GeV}} \right)^{-\alpha+1} = \frac{K}{(\alpha - 1)} \left(\frac{E}{1 \text{ GeV}} \right)^{-\gamma} \frac{\text{particles}}{\text{cm}^2 \text{ s sr}}. \quad (2.20b)$$

The parameter α is the *differential spectral index of the cosmic ray flux* (or the *slope* of the CR spectrum) and K a normalization factor; $\gamma \equiv \alpha - 1$ is the *integral*

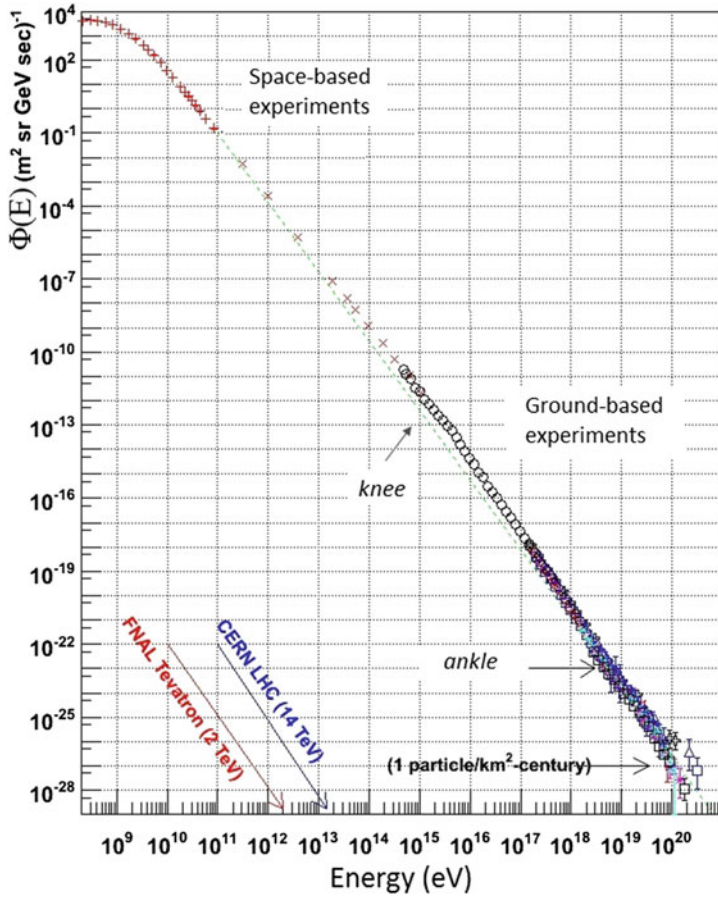


Fig. 2.7 The differential energy spectrum $\Phi(E)$ (units: particles/m² sr s GeV) of cosmic rays over eleven decades of energy. The red/blue arrows indicate the equivalent center of mass energy reached at the Tevatron collider at Fermilab and at the LHC collider at CERN. Note that the spectrum is remarkably continuous over the whole energy interval, and that the flux on the y-axis covers 33 decades. The dashed line shows a E^{-3} spectrum

spectral index. The numerical values of the parameters are determined through a fit to experimental data.

Different compilations of data exist which determine the parameters K, α using direct measurements of the CR flux (Chap. 3). These compilations give results in agreement within $\sim 30\%$. In the energy range from several GeV to $\sim 10^{15}$ eV, we use that obtained in Wiebel-Sooth et al. (1998), with

$$K = 3.01; \quad \alpha = 2.68 \quad (2.20c)$$

that includes the contribution of protons ($\sim 90\%$) and heavier nuclei. The compilation of Hörandel (2003) in the same energy region gives $K = 2.16$, $\alpha = 2.66$. The Beringer et al. (2012) gives the proton flux in terms of *energy-per-nucleon*, with $K = 1.8$, $\alpha = 2.7$.

The *energy-per-nucleon* is the *energy-per-nucleus*, divided by the number of nucleons. Conventionally, the two quantities can be distinguished by the indication that the energy-per-nucleus is measured in [GeV], while the energy-per-nucleon in [GeV/nucleon] or [GeV/A], where the “A” stands for “nucleons”. The energy-per-nucleon can be assessed only through *direct* experiments, when both E and $Z \sim A/2$ are measured. When the atmosphere is used as a calorimeter in air shower experiments, generally the energy-per-nucleus is measured.

Above the knee, the CR flux decreases by a factor ~ 100 when the energy increases by a factor of 10. The spectral index of the CR spectrum becomes steeper, $\alpha \sim 3.1$. The measurements of the CR spectrum above the knee are presented in Chap. 4. At the energy of $\sim 10^{10}$ GeV the spectrum becomes flatter again in correspondence of the second transition point, called the *ankle*. CRs above the ankle are thought to have an extragalactic origin (Chap. 7).

The *knee* and *ankle* structures are more evident in Fig. 2.8. It shows almost the same data set as in Fig. 2.7. The main difference is that the y-axis variable is multiplied

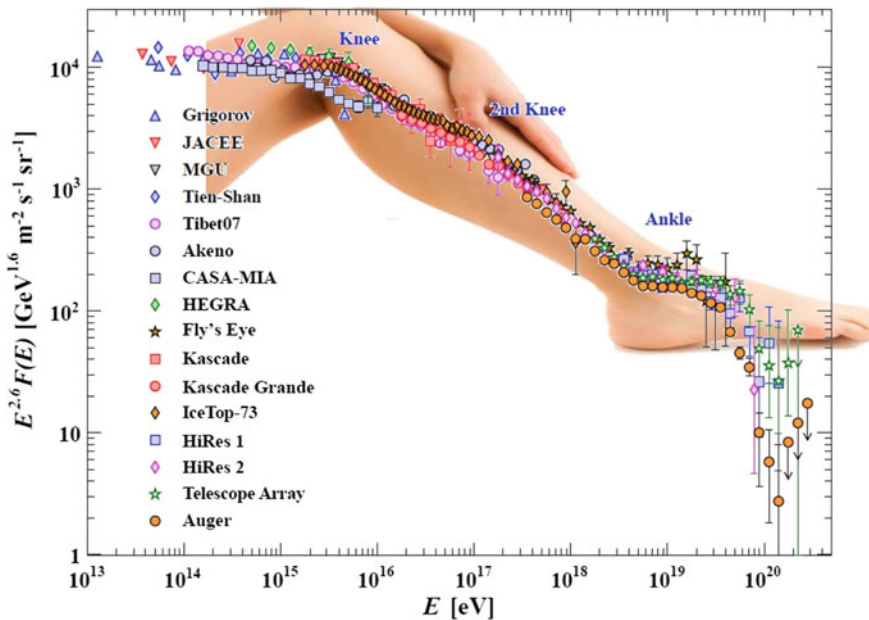


Fig. 2.8 The differential CR flux $\Phi(E)$ as measured by many *direct* and *indirect* CR experiments over eight decades of energy, almost the same as Fig. 2.7. Here the flux is multiplied by a power of the energy: $\Phi(E) \times E^{2.6}$. The structures of the knee and ankle are more evident as well as point-to-point differences between different experiments (most due to systematic uncertainties on the energy calibration). Adapted from a figure from Sect. 27: Cosmic Rays of Beringer et al. (2012)

by $E^{2.6}$. As explained in Sect. 1.2, this enhances the visibility for structures in the spectrum.

About 79 % of the primary nucleons are free protons and about 70 % of the rest are nucleons bound in helium nuclei (see Sect. 3.7). The flux of electrons corresponds to less than 1 % of that of protons and nuclei at the same energy. This does not correspond to a charge-asymmetry in the CR sources. Electrons (as explained in the following chapters) suffer larger energy losses that reduce the number of those arriving with high energies on Earth. In general, fluxes of CR particles as measured on Earth are influenced by their travel through the galactic interstellar medium and magnetic field. In the next section, a description of the main properties of the Galaxy is given.

2.7 The Physical Properties of the Galaxy

Today it is an established fact that the Sun is part of a system of stars, the *Galaxy* (or *Milky Way*), which is very similar to the spiral galaxies that we observe in the Universe. This conclusion was a sort of larger scale *Copernican revolution* and was thus a nontrivial fact, also from the observational point of view.

The determination of the shape and the size of the Galaxy with optical measurements only has been difficult because of the position of the solar system within the Galaxy. In this context, it was very important the observation of distant galaxies, which revealed large-scale structures that were not visible in our Galaxy, due to light absorption by interstellar dust. Only around 1930 it became unmistakably clear that the Galaxy is similar to objects at that time called *spiral nebulae*.

The recent images of the Galaxy using observations at different wavelengths show that it is basically a disk with a central bulge surrounded by a halo of globular clusters. It is convenient to distinguish two components: a *spheroidal* and a *disk* structure. Both contain stellar populations and other material with very different characteristics. These two components have different chemical compositions, kinematic and dynamic properties and a diverse evolutionary history.

Distances and sizes are usually expressed by astronomers in *parsec* (symbol: pc). One parsec corresponds to about 3.26 light-years or to

$$1 \text{ pc} = 3.086 \times 10^{18} \text{ cm} \quad (2.21)$$

The spheroidal component has a very massive nucleus (smaller than 3 pc of radius) with a *black hole* at its center, with mass $2 \times 10^6 M_{\odot}$,⁶ a bulge with radius of ~ 3 kpc and an extended halo of about 30 kpc. These three regions are approximately concentric. The disk is very thin (~ 200 – 300 pc thick) and a radius of about 15 kpc. The Sun is about 8.5 kpc from the center.

⁶ The subscript \odot conventionally represents the Sun and \oplus the Earth.

The galactic volume, assuming a flat disk having a radius of ~ 15 kpc and a thickness of ~ 300 pc, corresponds to:

$$\mathcal{V}_G = [\pi(15 \times 10^3)^2 \times 300] \times (3 \times 10^{18})^3 = 5 \times 10^{66} \text{ cm}^3 \quad (2.22)$$

The volume of the galactic halo is more than an order of magnitude larger.

Stars and globular clusters are the characteristic components of the spherical region, where gas and dust are relatively scarce. Spectroscopy indicates that the stars in the spheroid component are *metal-poor*⁷ (stars of population II). Metal-poor stars consist of material that has not undergone much recycling through previous generations of stars, are very old and represent the typical population of globular clusters.

The disk is instead characterized by the presence of large amounts of dust and gas, which give rise to absorption of the interstellar radiation, and by young and metal-rich stars (Population I). These stars may be distributed more or less uniformly, or grouped in stellar associations along the spiral arms. These considerations suggest that the disk is made entirely of materials already processed in previous generations of stars. This situation is analogous to that observed in other spiral galaxies.

An estimate of the total number of stars in the Galaxy is about 10^{10} .

Important information on the Galaxy have become available after the advent of radio astronomy. At low frequencies (150 MHz) the emission from the Galaxy shows a maximum of intensity along the galactic plane. The emission decreases steadily with increasing galactic latitude b ,⁸ covering the whole sky. The diffused radio emission is usually described in terms of two distinct structures. (i) a disk (which coincides with the optical disk) with an angular aperture of about $\pm 5^\circ$ in galactic latitude b ; (ii) an ellipsoidal shaped halo which extends at high galactic latitudes and up to the poles. From the study of the emission spectrum, it can be inferred that the diffuse radiation is composed of a nonthermal component and a thermal one from the disk. The nonthermal component is due to synchrotron radiation of electrons moving in the galactic magnetic field. The luminosity⁹ of the component from the disk, integrated over the whole radio band, is equal to:

$$\mathcal{L} \sim 10^{38} \text{ erg/s} . \quad (2.23)$$

The luminosity from the emission of the halo is subject to greater uncertainty, but corresponds (within a factor of 2) to that of the disk.

Superimposed to the thermal emission, discrete radio sources are observed. They are divided in two populations: (1) objects of large angular size, concentrated along

⁷ In the language of astronomers, all elements heavier than He are often called metals.

⁸ See *Extras # 2* for the astronomical coordinate systems.

⁹ In astronomy, the luminosity measures the total amount of energy emitted by a star or other astronomical object per unit time over the whole electromagnetic spectrum or a defined part of it.

the galactic plane; they are supernova remnants, surrounded by regions with a high concentration of ionized hydrogen. (2) radio sources of small angular diameter isotropically distributed and attributed to extragalactic objects. In both cases, the spectrum of the radiation is that typical of synchrotron emission.

2.7.1 The Galactic Magnetic Field

The presence of a magnetic field inside the Galaxy was discovered (1949) when it was realized that the observed light from the stars has a high degree of polarization. This polarization is correlated with the attenuation of starlight due to the presence of dust (Brown 2010).

Precise information on the galactic magnetic field comes from radio astronomy. Radio telescopes can measure the Faraday rotation angle and the extent of dispersion of the radiation emitted by pulsars and the Zeeman effect on the 21 cm line of neutral hydrogen.

The Faraday rotation effect is based on the fact that the plane of polarization of linearly polarized electromagnetic waves rotates when they propagate in the presence of a magnetic field B in a medium with electron density n_e [cm^{-3}]. The rotation depends on the square of the wavelength λ , and on the parallel component of the magnetic field B_{\parallel} along the line of sight to the source:

$$\text{RM} = \int_0^L B_{\parallel} n_e dr \quad (2.24)$$

where L is the distance traveled by the radiation. By measuring the variation of the angle of polarization as a function of the wavelength λ from radio pulsars, RM can be estimated. From independent estimates of n_e and L , the value of B in the traversed region can be deduced.

Different estimates exist on the average intensity of the regular galactic magnetic field, which depends on the distance from the galactic center (Fig. 2.9). We assume approximately:

$$B \simeq 4 \mu\text{G} \quad (2.25)$$

The galactic field is oriented mainly parallel to the plane, with a small vertical component along the z -axis ($B_z \sim 0.2\text{--}0.3 \mu\text{G}$ in the vicinity of the Sun).

The models of the large-scale structure of the galactic magnetic field provide a regular distribution of the \mathbf{B} lines that follows the distribution of matter, i.e. a spiral shape (Stanev 2010). The spatial extension of regions in which the magnetic field is coherent is of the order of 1–10 pc. Figure 2.10 shows the direction and strength of the regular magnetic field in the galactic plane. The large-scale structure of the galactic

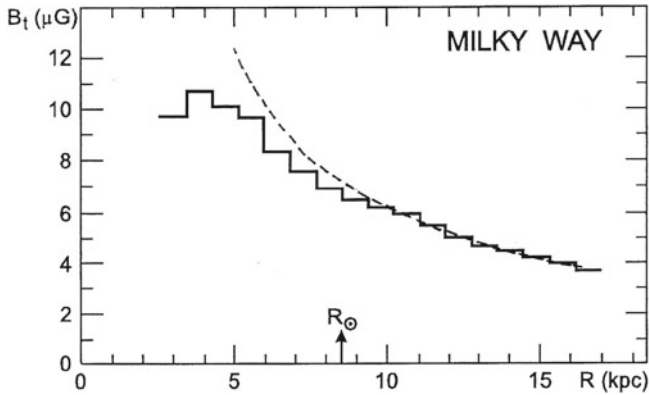
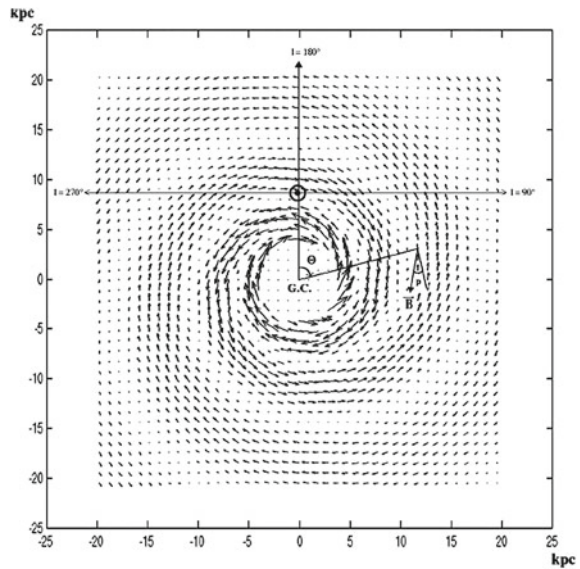


Fig. 2.9 Total magnetic field strength in the Galaxy as a function of the distance from the galactic center. The position of the Sun is indicated by the arrow (Battaner et al. 2007). Courtesy of Prof. E. Battaner

Fig. 2.10 The direction and strength of the regular magnetic field in the Galactic plane is represented by the length and direction of the arrows. The intensity of the field inside the circle of radius 4 kpc representing the bulge is assumed to be $6.4 \mu\text{G}$ (Prouza and Smída 2003). Courtesy Dr. M. Prouza and Dr. R. Smída



magnetic field strongly influences the motion of charged particles. An example of this influence on charged particles with three different energies is visible in Fig. 7.3.

An important problem, which is far from being solved, is the galactic magnetic halo, i.e., the extension of the magnetic field above and below the galactic plane. Recent measurements indicate an extended halo that can contribute significantly to the cosmic ray confinement.

As the Galaxy is filled with a magnetic field whose average intensity is $B \sim 4 \mu\text{G}$, we obtain using (2.5) the following Larmor radii for protons at different energies:

$$\begin{aligned}
r_L(E = 10^{12} \text{ eV}) &\simeq 10^{15} \text{ cm} = 3 \times 10^{-4} \text{ pc} \\
r_L(E = 10^{15} \text{ eV}) &\simeq 10^{18} \text{ cm} = 0.3 \text{ pc} \\
r_L(E = 10^{18} \text{ eV}) &\simeq 10^{21} \text{ cm} = 300 \text{ pc}
\end{aligned} \tag{2.26}$$

These values of r_L should be compared with the Galaxy dimensions. Particles below 10^{18} eV are strongly constrained inside the galactic volume by the galactic magnetic field.

2.7.2 The Interstellar Matter Distribution

In outlying regions of the Galaxy, the ratio of the distance between stars and their diameter is of the order of ~ 1 pc: $(10^6 \text{ km}) \simeq 3 \times 10^7$. Thus only a small fraction of the space ($\sim 4 \times 10^{-23}$) is occupied by matter in the form of stars. The rest is filled with large masses of gas (molecules, atoms, ions) and tiny solid particles, the interstellar dust. Dusts are made up of ice grains of various species, graphite, silicates and perhaps metals. The gas is revealed by the presence of absorption and emission lines, both in the optical and in radio. Dusts are observed only as large dark clouds obscuring the view of the stars behind, or in reflection nebulae which shine for the presence of nearby stars. Another tracer of the presence of dust is the infrared emission in the vicinity of very hot stars.

As a whole, this gas and dust is called *InterStellar Matter (ISM)*. It represents 5–10% of the total mass of the Galaxy. The average density of this medium is (Ferriere 2001)

$$n_{\text{ISM}} \sim 1 \text{ proton/cm}^3 = 1.6 \times 10^{-24} \text{ g/cm}^3 \tag{2.27}$$

It is hard to detect the ISM in the visible range of the electromagnetic radiation, and it has been studied mostly using radio-astronomy techniques. Most of the ISM is made of neutral (HI) and molecular (H_2) hydrogen.

Neutral hydrogen is the main component of the ISM, with an average density of approximately 0.4 atoms/cm^3 . The presence of HI is revealed in the radio band through the 21 cm line. The line was measured in emission mainly along the galactic plane, and with smaller intensity at all galactic latitudes. The linear dimension of the regions in which neutral hydrogen is present is of the order of 100–150 pc.

The emission is due to the fact that the ground state of the hydrogen atom consists of two hyperfine levels. They correspond to configurations with spin of the proton and electron parallel (higher level) and antiparallel (lower level). The emission is due to the transition between levels, whose energy difference corresponds to an electromagnetic emission with frequency $\nu_H = 1,420.40575 \text{ MHz}$, or $\lambda_H = 21.1049 \text{ cm}$. In thermodynamic equilibrium, the population of each level depends on its energy according to the Boltzmann law. The transition between the two levels has a lifetime $\tau \sim 1.1 \times 10^7 \text{ y}$. Although this corresponds to a very low transition probability, there is such a large quantity of hydrogen in the Galaxy that the line is clearly detectable.

In addition to the emission, the line can also be seen in *absorption* when a cloud of hydrogen is located on the line of sight between the observer and a radio source that emits a continuous spectrum.

About 1 % of interstellar hydrogen is ionized (HII). It is generally found in the form of clouds with a density that exceeds 10 atoms/cm^3 . The ionization is due to the presence of very hot stars that emit photons of energy larger than the ionization energy of hydrogen (13.6 eV). The HII emission is due to *free-free* (or *thermal bremsstrahlung*) transitions, which produces a continuous spectrum.

Radio telescopes have revealed the presence in the ISM of the characteristic lines of many molecules. Molecules emit through their vibrational modes. For example, the simple OH molecule can rotate with respect to the axis that joins the two nuclei, or around an axis perpendicular to it. The vibrational modes of the molecules are quantized, and this allows the identification of the molecules themselves.

About 50 % of the mass of the interstellar medium is in molecular form, and most of this seems to be H_2 . Unfortunately, the H_2 molecule has no rotational energy levels in the radio band, and the estimates of its presence in the Galaxy are rather uncertain. A large fraction is gathered in clouds, both compact and diffuse, with dimensions that reach 50 pc, and with high densities (up to $10^{10} \text{ molecules/cm}^3$). The temperatures of these clouds can reach up to thousands of degrees. These clouds correspond to the star forming regions.

In addition to the H_2 molecule, almost a hundred different molecules and molecular radicals were identified in the ISM. The more complex molecular systems have up to 13 atoms. Most of the complex molecules are organic. None of the inorganic molecules (except the ammonia, NH_3) contain more than three atoms. Apparently, as on Earth, the bond with carbon is the key for the formation of complex molecules!

One of the most interesting molecules detectable in the radio is the CO, which is the most abundant molecule after H_2 . It has three emission lines (with λ between 1 and 3 mm). The CO is a tracer for molecular hydrogen, because its main excitation source is due precisely to collisions with the H_2 molecule.

2.8 Low-Energy Cosmic Rays from the Sun

The Sun is the main source of CRs of energy below $\sim 4 \text{ GeV}$. Episodic solar activities and the corresponding increase of the low-energy CR flux have a number of effects that are of practical interest. A radiation dose from energetic particles is an occasional hazard for astronauts and for electronics on satellites.¹⁰ Such disturbances

¹⁰ I was always fascinated by “2001: A Space Odyssey”, a science fiction film produced and directed in 1968 by Stanley Kubrick. A space voyage to Jupiter tracing a signal emitted by an unknown object (a monolith) was organized with a spaceship. Most of spaceship’ operations are controlled by a computer on board, HAL 9000 (or simply “Hal”, as Hal interacts and speaks with the human crew), and double-checked by a twin computer on Earth. Hal states that he is “foolproof and incapable of error”. The main problem arises when Hal foresees an imminent failure on a device. The twin computer on Earth is of the contrary advice. Humans on board of the spaceship discover that Hal is

may damage power systems, disrupt communications, degrade high-tech navigation systems, or create the spectacular aurora.

Cosmic rays originated from the Sun were first observed in the early 1940s. They consist of protons, electrons, and heavy ions with energy ranging from a few tens of keV to few GeV. They are originated mainly by *solar flares*.

A solar flare is a sudden brightening observed over the Sun's surface, which is interpreted as a large energy release. Flares occur in active regions around sunspots, where intense magnetic fields penetrate the photosphere to link the corona to the solar interior.

The Sun activity influences also the probability that CRs with energy below few GeV reach the Earth. When CRs enter our solar system, they must overcome the outward-flowing *solar wind*. This wind is a stream of charged particles continuously released from the upper atmosphere of the Sun and it consists mostly of electrons and protons with energies usually between 1.5 and 10 keV.

The flux of galactic CR nuclei with energies below ~ 1 GeV/nucleon is strongly modulated by their interaction with the magnetic field carried by the expanding solar wind. The expanding magnetized plasma generated by the Sun decelerates and partially excludes the lower energy particles from the inner solar system. Consequently the low-energy component of the CR flux undergoes a sizable variation over the solar cycle. This effect is known as *solar modulation*.

The magnetic activity and the solar modulations are manifested through *sunspots*, which have a 11 *year cycle*. Most solar flares and coronal mass ejections originate in magnetically active regions around visible sunspot groupings. It should be noted that the earliest surviving record of sunspot observation dates from 364 BC, based on comments by Chinese astronomers (Early Astronomy and the Beginnings of a Mathematical Science, University of Cambridge, NRICH, 2007, <http://nrich.maths.org/6843>). From 28 BC, sunspot observations were regularly recorded by Chinese astronomers in official imperial records.

The intensity of low-energy CRs at Earth is measured through ground-based detectors called *neutron monitors*. Their measurements are anti-correlated with the level of solar activity, i.e., when solar activity is high many sunspots are visible, the CR intensity at Earth is low, and vice versa. Neutron monitors are designed to measure neutrons produced by the interactions of CRs with the atmospheric nuclei. If the primary CR that started the cascade has energy over ~ 500 MeV, some of its secondary by-products (including neutrons) will reach ground level. Figure. 2.11 shows the correlation between the number of observed sunspots (which measure the phase of the 11 y solar activity) and the number of neutrons detected at ground.

(Footnote 10 continued)

really wrong. They decide to disconnect it and to assign the spaceship operations to the computer on Earth. This decision induces a fight between humans and Hal. We are interested on the reason why there is a *discrepancy* between the prevision of the failure carried out by Hal and by the twin computer on Earth. The only plausible reason is the fact that the processor units of the Hal on board of the spaceship were damaged by cosmic rays. Although it is a science fiction movie, it fully grasped one of the main problems for long time permanence of humans in space. Computer failures can be prevented by increasing the number of units. This solution cannot be adopted for humans.

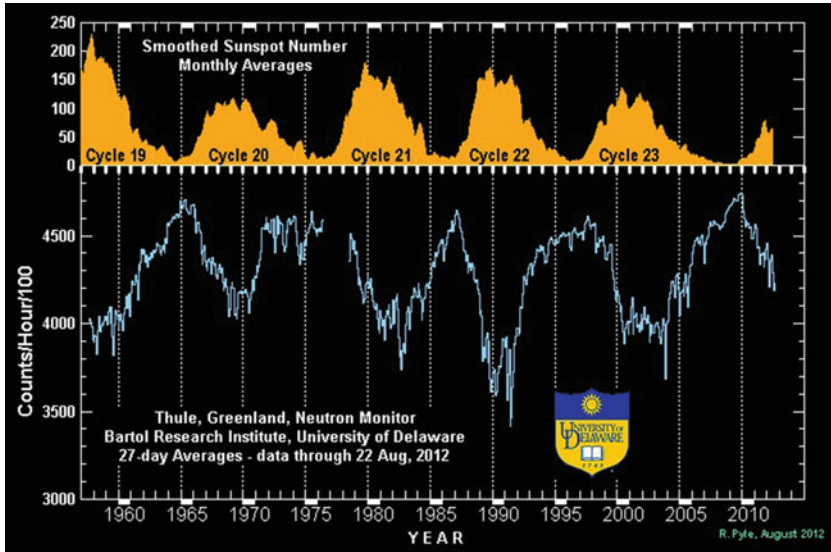


Fig. 2.11 The solar modulation cycle (<http://www.bartol.udel.edu/gp/neutronm/>). The rate of the neutron monitor is updated monthly), which correlate the sunspot number (on the *top*) with the neutron rate measured at the McMurdo station (*bottom* of the figure). *Credit* the Bartol Research Institute

The correlation of the CR flux for energies below few GeV with the solar phase is clearly visible in Fig. 2.12. Here, the flux of protons as measured by the PAMELA experiment (Sect. 3.4.2) in four different years is shown (Adriani 2013). A higher proton flux at energies below few GeV is evident during 2009, when the number of monthly sunspots in Fig. 2.11 was almost zero.

2.9 The Effect of the Geomagnetic Field

To reach the top of the atmosphere, particles and nuclei below the GeV range are guided by the Earth dipolar magnetic field. Thus the intensity of any low-energy component of the cosmic radiation depends both on the location and time.

For certain magnetic field configurations, there exist regions of space for which the arrival of particles below a certain energy threshold is forbidden. These regions of space are said to be shielded from such particles. Using the concept of a magnetic potential barrier, Störmer showed first (around the 1920s) the existence of a shielded region for the Earth dipole magnetic field configuration. A simple condition which is necessary for a particle to reach the Earth atmosphere is that all trajectories starting from the point considered on Earth (after reversing the charge of the particle) reach $r = \infty$. At low enough energies, this condition may be violated, because trajectories

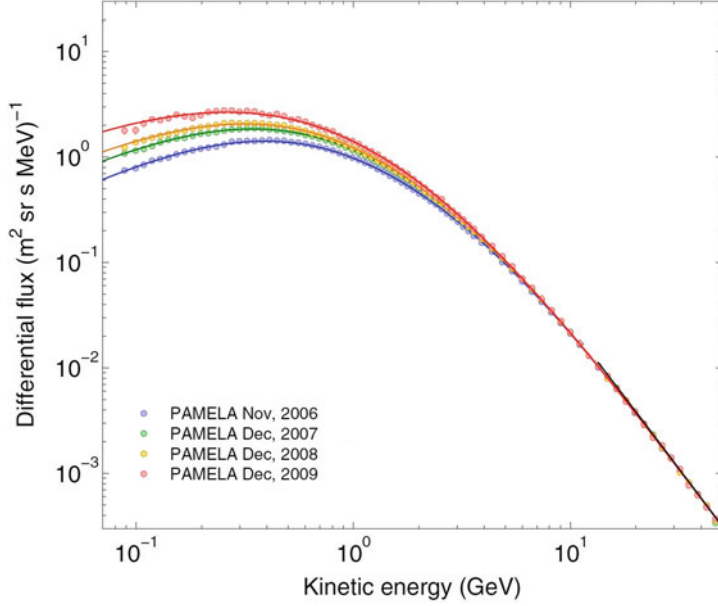


Fig. 2.12 The yearly proton energy spectrum measured by the PAMELA experiment (Sect. 3.4.2) from the beginning of the space mission in mid of 2006 till end of 2009. Compare the phase of the solar activity with Fig. 2.11. The variation of the solar activity does not affect CRs with energy larger than few GeV. Courtesy of the PAMELA collaboration

can be deflected back to the Earth or stay within a finite distance. In this case, the magnetic field does induce anisotropies in the observed flux.

Consider a particle of charge Ze with orbit in the equatorial plane of the dipole-like Earth magnetic field. Equating the centrifugal and the Lorentz force gives (note that we express the following equations in the I.S. units):

$$\frac{mv^2}{r} = Ze|\mathbf{v} \times \mathbf{B}| \quad (2.28)$$

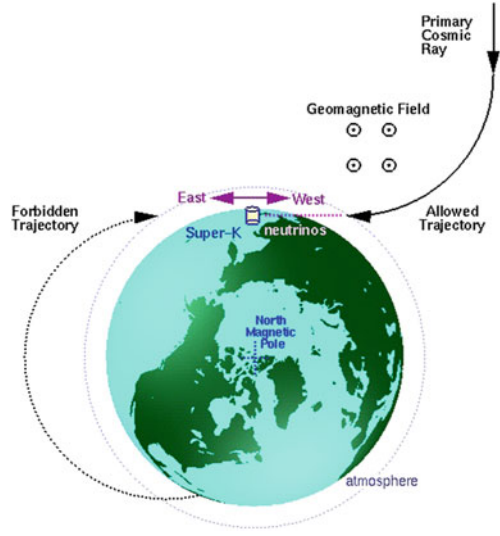
The Earth magnetic field is induced by the Earth magnetic moment \mathcal{M} :

$$B = \frac{\mu_0}{4\pi} \frac{\mathcal{M}}{r^3} \quad (2.29)$$

At the surface ($r = R_{\oplus} = 6.38 \times 10^6$ m) the measured value is $B = 0.307 \times 10^{-4}$ T, therefore $\mathcal{M} = 7.94 \times 10^{22}$ Am². It is easy work out from (2.28) and (2.29) the radius of the orbit:

$$r = \left(\frac{\mu_0}{4\pi} \frac{Ze\mathcal{M}}{p} \right)^{1/2} \quad (2.30)$$

Fig. 2.13 Primary CRs with energy below ~ 60 GeV are influenced by the Earth magnetic field. In particular, low-energy cosmic rays from the East are suppressed compared to those from the West. The Earth itself effectively shadows certain trajectories, which are therefore forbidden (Futagami et al. 1999). This East-West effect was first detected in the 1930s and was used to infer that the charge sign of the primary cosmic rays is positive. Courtesy of Prof. E. Kearns



where p is the particle momentum. Using the numerical values for $r = R_{\oplus}$:

$$\frac{p}{Ze} = \frac{\mu_0}{4\pi} \frac{\mathcal{M}}{R_{\oplus}^2} \sim 59.6 \text{ GV}. \quad (2.31)$$

This value corresponds to the minimum rigidity for a particle to be able to reach the Earth from the East, if its orbit is exactly in the (magnetic) equatorial plane (see Fig. 2.13). In fact, the radius of curvature of the trajectory labeled as *forbidden trajectory* does not reach ∞ starting from ground. Toward the poles, the influence of the dipole field becomes weaker (as the arriving particle velocity is almost parallel to \mathbf{B}), and the cutoff rigidity (2.31) becomes smaller. The integrated CR intensity increases with the latitude for charged particles (*latitude effect*). This is exactly the property measured by Compton in 1932 which demonstrated that CRs are positively charged (as we mentioned in Sect. 2.1). The East-West effect influences also the production of low-energy atmospheric neutrinos detected in underground experiments (Chap. 11).

The Earth dipole-like magnetic field induces also another relevant effect known as the *Van Allen radiation belts* (named after its discoverer, J. Van Allen). They are two torus-shaped layers of energetic charged particles around the Earth, located in the inner region of the magnetosphere, and held in place by the magnetic field, Fig. 2.14. The belt extends from an altitude of about 1,000–60,000 km above the surface. The outer belt consists mainly of energetic electrons, while the inner belt is formed by a combination of protons and electrons. The belts pose a hazard to satellites, which must protect their sensitive components with adequate shielding if their orbit spends a significant time inside the radiation belts.

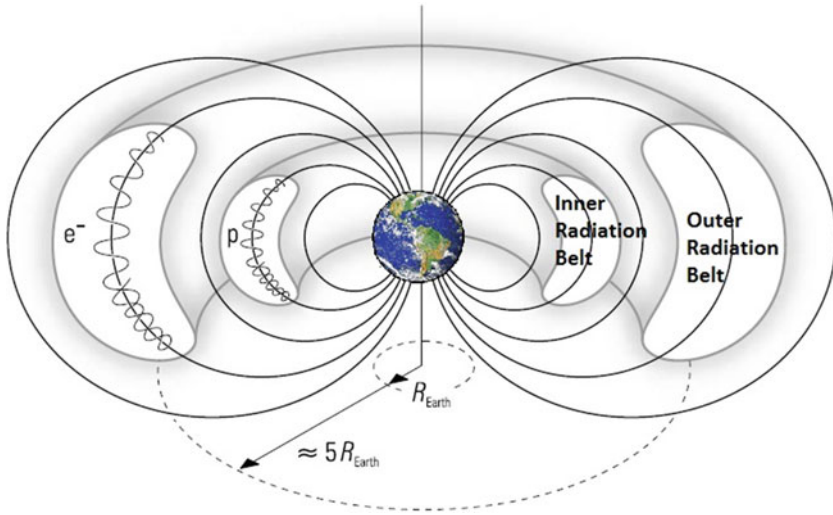


Fig. 2.14 Sketch of the van Allen radiation belts

2.10 Number and Energy Density of the Cosmic Rays

After this long journey in the environment in which CR propagate, let us now evaluate the number density of CRs, according to the definition (2.18a) for $v \simeq c$. We use the experimental flux as parameterized in (2.20b):

$$n_{\text{CR}} = \frac{4\pi}{c} \Phi(>E_0) = \frac{4\pi \cdot K/(\alpha - 1)}{3 \times 10^{10}} \cdot E_0^{-\gamma} \quad (2.32a)$$

The numerical value depends on the threshold energy E_0 . We assume that the parameterization (2.20a) holds down to $E_0 \simeq 3 \text{ GeV}$ where (somewhat arbitrarily) we put the threshold for the solar wind's contribution. This is confirmed also from Fig. 2.12 which shows no dependence on solar modulations for energies larger than this threshold. Using the values of (2.20c) and $E_0 = 3 \text{ GeV}$:

$$n_{\text{CR}} \simeq 1 \times 10^{-10} \text{ cm}^{-3} \quad (2.32b)$$

A second important quantity is the *kinetic energy density* (or, simply, the *energy density*) of CRs. It can be obtained by the integration of (2.13) assuming the flux given by (2.20a):

$$\begin{aligned}
\rho_{\text{CR}} &\equiv \frac{1}{c} \int_{E_0}^{\infty} E \frac{d^2\varphi}{dE d\Omega} dE d\Omega \quad [\text{GeV cm}^{-3}] \\
&= \frac{4\pi}{c} \int_{E_0}^{\infty} 3.01 E^{-\alpha+1} dE = \frac{4\pi}{c} \left[\frac{3.01}{\alpha-2} E^{-\alpha+2} \right]_{E_0}^{E_0} \quad (2.33a)
\end{aligned}$$

The numerical value depends on the threshold energy E_0 . As above using $E_0 = 3$ GeV we obtain:

$$\rho_{\text{CR}} \simeq 1 \text{ eV/cm}^3. \quad (2.33b)$$

We need to compare (2.32b) and (2.33b) with some other astrophysical quantities, in order to understand if they represent “small” or “large” quantities. The number density (2.32b) of CRs can be compared with the average number density of the interstellar matter (2.27). Thus, only about one proton out of $\sim 10^{10}$ not bound in stars in the Galaxy is a relativistic particle, i.e. a cosmic ray.

Concerning the energy density (2.33a), let us consider the following astrophysical quantities.

The energy density of the interstellar magnetic field. To any magnetic field region is associated a corresponding energy density that in the Gauss system corresponds to:

$$\rho_B = \frac{1}{8\pi} B^2 \text{ erg/cm}^3 \quad (2.34)$$

(the relation in the I.S. is $1/(2\mu_0) B^2 \text{ J/m}^3$). Using the numerical values for the average interstellar magnetic field ($B \sim 4 \mu\text{G}$) we obtain:

$$\rho_B = \frac{(4 \times 10^{-6})^2}{8\pi} = 6 \times 10^{-13} \text{ erg/cm}^3 \simeq 1 \text{ eV/cm}^3 \quad (2.35)$$

The coincidence within a small factor between (2.33b) and (2.35) suggests a connection between galactic magnetic field and CRs.

The starlight density. From photometric measurements of the light coming from galactic stars, astronomers have evaluated the visible photon density:

$$n_{\gamma_{\text{vis}}} \sim 2 \times 10^{-2} \text{ cm}^{-3} \rightarrow \rho_{\gamma_{\text{vis}}} \sim 4 \times 10^{-2} \text{ eV/cm}^3 \quad (2.36)$$

assuming 2 eV/photon for the visible light. This is a much smaller value than (2.33b)

The density of the Cosmic Microwave Background Radiation. The CMB radiation is the thermal radiation filling almost uniformly the observable Universe. A precise measurement of CMB radiation is extremely important to cosmology, since any proposed model of the Universe must explain this radiation. The CMB radiation has a thermal black body spectrum at a temperature of 2.725 K (Fixsen 2009),

which corresponds to an energy of $E_{\text{CMB}} \sim 3kT = 7 \times 10^{-4} \text{ eV}$, where $k = 8.61 \times 10^{-5} \text{ eV K}^{-1}$ is the Boltzmann constant. Using the measured number density of the CMB radiation:

$$n_{\gamma\text{CMB}} \sim 400 \text{ cm}^{-3} \rightarrow \rho_{\gamma\text{CMB}} \sim 0.3 \text{ eV/cm}^{-3}. \quad (2.37)$$

In this particular case, in spite of the similarity between (2.33b) and (2.37), there is no argued connection between the two phenomena.

2.11 Energy Considerations on Cosmic Ray Sources

Supernova remnants are energetically suitable candidates for the acceleration of CRs with energy below the knee. The main motivation is the equilibrium (firstly hypothesized by Baade and Zwicky in 1934) between the loss of CRs due to their escape out of the galactic volume and the energy provided by supernova shock waves.

The Galaxy is uniformly filled with the relativistic radiation we detect on Earth. The CR sources are uniformly distributed in the Galaxy and the CRs are trapped by the galactic magnetic fields. According to the present observations, the total kinetic energy of CRs corresponds to:

$$\rho_{\text{CR}} \times \mathcal{V}_G = 8 \cdot 10^{54} \text{ erg}. \quad (2.38)$$

where the energy density ρ_{CR} is given in (2.33b) and the galactic volume ($\mathcal{V}_G \sim 5 \times 10^{66} \text{ cm}^3$) in (2.22). If the particles are completely confined inside the galactic volume, this number should increase with time in the presence of new galactic core-collapse supernova explosions. This process that represents the candidate injection mechanism for galactic CRs have started very long time ago, as discussed in Chap. 6. Each supernova burst contribute to increase the galactic CR density ρ_{CR} . A competitive effect which induces a decrease of ρ_{CR} is due to the escape of CRs out of the Galaxy with a characteristic *escape time* (or *confinement time*) τ_{esc} . This quantity corresponds to the average time needed for a CR, trapped by the galactic magnetic field, to reach the galactic boundary. From here, the particle can freely escape, because the magnetic field outside the galactic plane is negligible.

Anticipating the results which we derive in Sect. 5.2, the confinement time is $\tau_{\text{esc}} \simeq 10^7 \text{ y} = 3 \times 10^{14} \text{ s}$. Assuming an almost steady value of the energy density ρ_{CR} , the energy loss rate due to the escape of CR out of the galactic volume is:

$$P_{\text{CR}} \simeq \frac{\rho_{\text{CR}} \times \mathcal{V}_G}{\tau_{\text{esc}}} = \frac{8 \cdot 10^{54}}{3 \cdot 10^{14}} = 3 \times 10^{40} \text{ erg/s}. \quad (2.39)$$

Thus, the power required by cosmic accelerators to replenish the galactic volume corresponds to P_{CR} .

This number has a large uncertainty. The assumption of $\rho_{\text{CR}} \sim \text{const}$ for a time scale $\gg \tau_{\text{esc}}$ is completely reasonable from the astrophysical point of view. It is not expected a large variation in the supernova rate in the last, say, billion years. Another uncertainty arises from the galactic volume, which is bigger if the *magnetic halo* is considered. As this magnetic field is poorly known, a galactic volume about $10\% V_G$ could be considered. In this case, the matter density in this extended volume is a factor of ~ 3 smaller. Compressively, the quantity estimated in (2.39) could be a factor of three larger, and $P_{\text{CR}} \simeq 10^{41}$ erg/s. Are these powers energetically compatible with the energy released by supernova explosions?

A supernova explosion of 10 solar masses ($10 M_{\odot}$) releases about 10^{53} erg, 99 % in form of neutrinos (Sect. 12.10) and 1 % in form of kinetic energy of expanding particles (shock wave). The supernova rate f_{SN} in a galaxy like our own is about 3 per century ($f_{\text{SN}} \sim 10^{-9} \text{ s}^{-1}$). If a physical process able to accelerate charged particles exists, it transfers energy from the kinetic energy of the shock wave to CRs with an efficiency η :

$$P_{\text{SN}} \simeq \eta \times f_{\text{SN}} \times 10^{51} = \eta \times 10^{42} \text{ erg/s.} \quad (2.40)$$

By requiring that $P_{\text{CR}} = P_{\text{SN}}$, the quantity η must be of the order of a few percent. In this case, the shock waves from supernova explosions are able to refurbish the Galaxy with new accelerated particles and maintain the stationary energy content of CRs. This condition makes the supernova model energetically compatible with the observations. A transfer mechanism with efficiency of few % is known and it will be described in Sect. 6.2. With a rate of about three supernovae per century in a typical Galaxy, the energy required could be provided by a small fraction ($\sim 5\text{--}10\%$) of the kinetic energy released by supernova explosions.

References

- O. Adriani et al., Time dependence of the proton flux measured by PAMELA during the 2006 July-2009 December solar minimum. *Astrophys. J.* **765**, 91 (2013)
- C. Anderson, The positive electron. *Phys. Rev.* **43**, 491 (1933)
- P. Auger et al., Extensive cosmic-ray showers. *Rev. Mod. Phys.* **11**, 288–291 (1939)
- W. Baade, F. Zwicky, Remarks on Super-Novae and cosmic rays. *Phys. Rev.* **46**, 76 (1934)
- E. Battaner et al., Magnetic fields in galaxies, in lecture notes and essays in astrophysics. III Astrophysics Symposium (2007), <http://www.slac.stanford.edu/econf/C07091016/>
- J. Beringer et al. (Particle Data Group), The review of particle physics. *Phys. Rev. D* **86**, 010001 (2012). <http://pdg.lbl.gov/>
- S. Braibant, G. Giacomelli, M. Spurio, *Particle and Fundamental Interactions* (Springer, Berlin, 2011). ISBN 978-9400724631
- J.C. Brown, The magnetic field of the milky way galaxy (2010), [arXiv:1012.2932v1](https://arxiv.org/abs/1012.2932v1)
- P. Carlson, A. De Angelis, Nationalism and internationalism in science: the case of the discovery of cosmic rays. *Eur. Phys. J. H* **35**, 309–329 (2010)
- K. Ferriere, The interstellar environment of our galaxy. *Rev. Mod. Phys.* **73**, 1031–1066 (2001)

- D.J. Fixsen, The temperature of the cosmic microwave background. *Astrophys. J.* **707**(2), 916–920 (2009), doi:[10.1088/0004-637X/707/2/916](https://doi.org/10.1088/0004-637X/707/2/916)
- T. Futagami et al. (The SK Collab.), Observation of the East-West anisotropy of the atmospheric, neutrino flux. *Phys. Rev. Lett.* **82**, 5194–5197 (1999). <http://hep.bu.edu/superk/ew-effect.html>
- J.R. Hörandel, On the knee in the energy spectrum of cosmic rays. *Astropart. Phys.* **19**, 193–220 (2003)
- J. Linsley, Evidence for a primary cosmic-ray particle with energy 10^{20} eV. *Phys. Rev. Lett.* **10**, 146 (1962)
- D. Pacini, La radiazione penetrante alla superficie ed in seno alle acque. *Nuovo Cimento VI/3* (1912) 93. Translated and commented by Alessandro De Angelis: Penetrating radiation at the surface of and in water. [arXiv:1002.1810](https://arxiv.org/abs/1002.1810)
- M. Prouza, R. Smída, The galactic magnetic field and propagation of ultra-high energy cosmic rays. *Astron. Astrophys.* **410**, 1–10 (2003)
- M. Schein, W.P. Jesse, E.O. Wollan, The nature of the primary cosmic radiation and the origin of the mesotron. *Phys. Rev.* **59**, 615–633 (1941)
- T. Stanev, *High Energy Cosmic Rays* (Springer Praxis Books, 2010). ISBN 9783540851486
- B. Wiebel-Sooth, P.L. Biermann, H. Meyer, Cosmic rays. VII. individual element spectra: prediction and data. *Astron. Astrophys.* **330**, 389–398 (1998)

Particles and Astrophysics
A Multi-Messenger Approach

Spurio, M.

2015, XVI, 491 p. 190 illus., 49 illus. in color., Hardcover

ISBN: 978-3-319-08050-5